

Full length article

Mechanism of the $\text{Fe}_3(\text{B,C})$ and $\text{Fe}_{23}(\text{C,B})_6$ solid-state transformation in the hypoeutectic region of the Fe–C–B system



Jonathan Lentz*, Arne Röttger, Werner Theisen

Ruhr-Universität Bochum, Institut für Werkstoffe, Lehrstuhl Werkstofftechnik, Universitätsstraße 150, D-44801, Bochum, Germany

ARTICLE INFO

Article history:

Received 1 June 2016

Received in revised form

1 August 2016

Accepted 2 August 2016

Keywords:

Fe–C–B

Ternary alloys

Boron

Steel

Solid state phase transformation

ABSTRACT

This study investigates the microstructural mechanisms involved in the solid-state transformation of the $\text{Fe}_3(\text{B,C}) \rightarrow \text{Fe}_{23}(\text{C,B})_6$ phases in the hypoeutectic region of the iron–carbon–boron (Fe–C–B) system. We analyzed the influence of different initial microstructural characteristics on the $\text{Fe}_3(\text{B,C}) \rightarrow \text{Fe}_{23}(\text{C,B})_6$ transformation with regards to the matrix phase, matrix C content, $\text{B}/(\text{C} + \text{B})$ ratio, and agglomeration of the parental $\text{Fe}_3(\text{B,C})$ phase. We performed thermodynamic calculations using the CALPHAD method, validated by laboratory melts with varying $\text{B}/(\text{B} + \text{C})$ ratios. These laboratory melts were then microstructurally characterized by means of X-ray diffraction (XRD), scanning electron microscopy (SEM), electron backscatter diffraction (EBSD), and wavelength-dispersive X-ray spectroscopy (WDS). We particularly focused on solid-state transformation of borides and carboborides of type $\text{M}_3(\text{C,B})$ and $\text{M}_{23}(\text{C,B})_6$ in the hypoeutectic region of the ternary system Fe–C–B, investigated via both *in situ* and *ex situ* XRD measurements. It was found that the solid-state transformations are influenced by enriched B inside the eutectic structure, a result of solidification. This increased B content is not reduced in solid state due to the kinetic limitations of B and C inside the hard-phase structure. Thus phase stability is subject to local equilibria depending on the local C and B concentration of the hard-phase structure. In this process the $\text{Fe}_{23}(\text{C,B})_6$ phase also forms a shell-like structure surrounding the $\text{Fe}_3(\text{B,C})$ and Fe_2B phases.

© 2016 Acta Materialia Inc. Published by Elsevier Ltd. All rights reserved.

1. Introduction

Tool components used in mining or materials processing need to resist high abrasive wear. The most cost-effective materials for this application are tool steels and wear-resistant cast irons, featuring a high hardness and a sufficient toughness, simultaneously. One challenge of modern alloy development is optimizing application properties, such as wear resistance and toughness, while increase cost effectiveness in terms of tool manufacture, maintenance, and lifespan. From a microstructural perspective, high wear resistance is the result of a sufficient volume fraction of hard phases, formed primarily or eutectically during the solidification sequence. These hard phases are embedded in and supported by a metallic matrix, which therefore requires high strength and toughness. Wear resistance can be optimized by tailoring the properties of the hard phases to the tribological interaction. Thus the most important parameters influencing wear protection performance are parameters relating to the distribution, morphology, and micromechanical

properties of the hard phases, such as hardness, Young's modulus, and fracture toughness. In this context, a comparison of different types of hard phases (carbides, nitrides, and borides) shows that borides generally display better micromechanical properties due to their high hardness and adequate fracture toughness. For example, it was shown that boron–cementite $\text{Fe}_3(\text{B,C})$ (hardness 1300–1400 HV0.05) or $(\text{Fe,Cr})_2\text{B}$ (hardness 1600–2000 HV0.05) have hardness of the same order of magnitude or even higher than that of Cr-rich carbides of type M_7C_3 (hardness 1400–1600 HV) [1–3]. In addition, these borides are based on the ternary alloying system Fe–C–B, which allows a reduction in the amount of more expensive but commonly alloyed hard-phase forming elements such as Cr, Mo, V, or W. Hence, boron (B) seems a promising hard-phase forming element for a novel alloying approach for tool steels or white cast iron.

However, the current state of research shows controversial or limited results for phase stability and phase formation mechanisms for the hypoeutectic alloying region of the ternary system Fe–C–B. There is particular disagreement surrounding the formation mechanisms and stability region of the $\text{Fe}_{23}(\text{C,B})_6$ phase (τ -phase). For instance, the stable temperature region for the $\text{Fe}_{23}(\text{C,B})_6$ phase

* Corresponding author.

E-mail address: Jonathan.Lentz@Ruhr-Uni-Bochum.de (J. Lentz).

was found to lie in a wide temperature range from 600 to 950 °C in solid state. In contrast, some authors reported primary stability and eutectic solidification at temperatures higher than 1100 °C. A brief summary can be found in the literature [4], which considers the differences in the experimental setup of the various studies, such as melt size and quenching rates. In this context, the strong segregation effects of B and rapid non-equilibrium solidification processing shift the phase field of the liquid phase to lower temperatures and thus enable crystallization of the τ -phase from the melt. In addition, it was found that alloying elements like chromium increase the stability of the τ -phase and thus shift the formation of the τ -phase to higher temperatures close to the solidus temperature [1].

From a technical perspective, B additions in the order of 50–100 ppm are used to form small precipitations of the B-bearing τ -phase (around 100 nm in size) in low-alloyed ferritic/martensitic steels to increase creep resistance [5–7]. Furthermore, B grain boundary segregation and precipitation of the τ -phase on grain boundaries is discussed in the context of reducing the interfacial energies of γ -Fe grains, thus retarding the nucleation of α -Fe and increasing hardenability, e.g., for press-hardening steels for automotive use [8–10]. For wear protection, B is alloyed in the order of magnitude of 1 mass% to promote the formation of hard borides and carboborides. In the hypoeutectic region of the ternary system Fe–C–B, the three Fe-rich hard phases of type $\text{Fe}_3(\text{B,C})$, Fe_2B , and $\text{Fe}_{23}(\text{C,B})_6$ are known. In this context, the τ -phase ($\text{Fe}_{23}(\text{C,B})_6$) displays lower hardness (hardness 1100 HV0.05) than the $\text{Fe}_3(\text{B,C})$ (hardness 1400 HV0.05) and Fe_2B (hardness > 1600 HV0.05) hard phases, which are therefore preferred. However, the formation of the $\text{Fe}_{23}(\text{C,B})_6$ phase and its interrelation with the transformation of $\text{Fe}_3(\text{B,C})$ and Fe_2B hard phases is a precondition for successful alloy development in the Fe–C–B system. A previous study investigated the solidification behavior of the hypoeutectic region of the Fe–C–B system in this context [11]. It was found that, subsequent to primary crystallization of γ -Fe matrix phase, the Fe_2B and $\text{Fe}_3(\text{B,C})$ hard phases are continuously solidifying due to a eutectic transition reaction and forming a network-like structure. Furthermore, the $\text{Fe}_{23}(\text{C,B})_6$ phase was not found to crystallize from the melt.

A deeper understanding of the formation mechanisms of the τ -phase is motivated by the technical utilization of B as an alloying element in tool steels and to create a basis for a targeted microstructural tailoring of tool steels based on the hypoeutectic region of the Fe–C–B system. However, numerous influencing parameters are involved in the τ -phase formation mechanisms and the solid-state transformations occurring in the underlying hypoeutectic region of the ternary Fe–C–B alloying system. This high complexity of the mechanism of action complicates investigations and has led to contradictory observations being published. As a result, the following investigations focus on the ternary Fe–C–B system and ignore the influence of additional alloying elements. This study aims to characterize the phase formation mechanisms of the $\text{Fe}_{23}(\text{C,B})_6$ phase, which is formed in a temperature close to the austenite–ferrite–transition temperature (700–1000 °C). Particular focus is placed on the formation processes taking place in the region of the eutectic hard-phase structures rather than small precipitates for example on grain boundaries, as the former are relevant for wear protection.

2. Experimental procedure

2.1. Production of laboratory melts and specimens

Laboratory melts from the hypoeutectic region of the Fe–C–B system were cast and experimentally characterized. The effect of increasing B content was reproduced through systematic variation of the laboratory melt's B content between 0.2 and 1.4mass%. To

establish the basis for a prospective alloy design for tool steels, the carbon (C) content was kept constant at 0.6 mass% to maintain martensitic hardenability of the iron matrix. Accordingly, the B/(C + B) ratio was varied between 0.25 and 0.7, as shown in Table 1.

For this purpose, the compounds FeB, electrolytic Fe, and raw iron were weighed in amounts of 200 g and melted in alumina crucibles using a vacuum induction furnace with argon atmosphere of 1 bar present. The chemical composition of the laboratory melts was validated using Optical Emission Spectroscopy (OES) (see Table 1).

Specimens were cut from the casting using a CBN cutting disc. The phase stability was investigated at temperatures of 700, 800, 900, and 1000 °C. To adjust phase stability of the high temperature condition, specimens were tempered in a vacuum furnace at 700, 800, 900, and 1000 °C for 366 h and subsequently quenched in water to freeze the high temperature microstructure. In the following, the particular specimens will be designated using the alloying composition and tempering temperature (e.g., 0.2B–0.6C–700 °C).

2.2. Thermodynamic calculations

Thermodynamic equilibrium calculations based on the CALPHAD method were performed to calculate phase and property diagrams using Thermo-Calc software version 4.1. Thermodynamic data were taken from the TCFE7 database, considering the liquid phase (LIQUID), ferrite (B2_BCC), austenite (FCC_A1), $\text{Fe}_{23}(\text{C,B})_6$ (M23C6), $\text{Fe}_3(\text{B,C})$ (CEMENTITE), Fe_2B (M2B_TETR), FeB (BM), and B_4C (B4C). The simulation was run with a pressure and quantity of $p = 10^3$ mbar and $n = 1$ mol, respectively.

2.3. Metallography & microstructural characterization

The metallographic preparation was performed by embedding the samples in Cu-based conductive polymer Technovit5000, followed by a stepwise grinding with SiC paper from 80 to 1000 mesh and polishing using 54 μm –1 μm diamond suspension. The microstructure of the specimens was contrasted by etching the samples with 3% alcoholic HNO_3 acid.

For microstructural characterization, a scanning electron microscope (SEM) (MIRA3, Tescan) with secondary-electron (SE) and back-scatter-electron (BSE) detector was used at an acceleration voltage of 20 kV and a working distance of 8 mm. Quantitative phase analysis was performed via image binarization. Five images per specimen were taken using the SE detector and subsequently analyzed using A4i (Archive4Images) analysis software. Electron backscattered diffraction (EBSD) measurements were performed for samples tilted for 70° using an Oxford Nordlys nano detector. Noise inside the EBSD maps resulting from indexing problems of the cubic (super-)lattice structures of the α -Fe and $\text{Fe}_{23}(\text{C,B})_6$ phases was reduced through digital smoothing. Quantitative measurements of the chemical composition of the hard phases were carried out via wavelength dispersive spectrometry (WDS) using a microprobe (CAMECA, SX5-FE). Certified reference materials were used to standardize the elements B (using B_4C), C and Fe (using Fe_3C). WDS measurements were performed at an acceleration

Table 1
OES measurements of the alloy composition in mass%.

Alloy	B/(C+B)-ratio	C	B	Mn	Si	Fe
0.2B–0.6C	0.25	0.53	0.19	0.09	0.19	Bal.
0.6B–0.6C	0.5	0.56	0.55	0.01	0.15	Bal.
1.4B–0.6C	0.7	0.61	1.48	0.10	0.26	Bal.

voltage of 10 kV and a beam-current of 40 nA, with a cooling trap ($T = -196\text{ }^{\circ}\text{C}$) used to prevent C-contamination during electron irradiation.

2.4. Phase analysis

Phase analysis was performed using an X-ray diffractometer (D8 Advance, Bruker) with Bragg-Brentano configuration. Polished samples (finished with $1\text{ }\mu\text{m}$ diamond suspension) with a surface area of $10 \times 10\text{ mm}$ were irradiated with $\text{Cu K}\alpha$ radiation. Reflections were recorded in an angular range from 35 to $85\text{ }2\theta^{\circ}$, a step size of $0.1\text{ }2\theta^{\circ}$, and a holding time of 10 s per increment; the specimens were rotated during the irradiation to minimize texture effects. The diffraction peak patterns were analyzed using DIFFRAC.EVA software and the JCPDS-database PDF-2.

High-temperature *in situ* phase analysis was performed to investigate the temperature and time dependent formation of the $\text{Fe}_{23}(\text{C,B})_6$ phase. To achieve this, a heating chamber (Anton Paar, HTK) was adapted to the X-ray diffractometer (D8 Advance, Bruker). Polished specimens ($1\text{ }\mu\text{m}$ diamond suspension finish) with a surface area of $10 \times 10\text{ mm}$ and a thickness of 1 mm were placed upon a Pt heating element, heated by electrical current flow. The temperature of the specimen surface was controlled by an attached Pt-PtRh thermocouple. Prior to heating cycles, the chamber was repeatedly evacuated and vented with 99.9999% pure He gas. The experiments were then performed with a static excess pressure of 300 mbar He atmosphere to prevent contamination by oxygen or nitrogen. While passing particular temperature time steps, diffractograms were recorded in intervals of 240 s within an angular range from 42 to $46\text{ }2\theta^{\circ}$ and a step size of $0.1\text{ }2\theta^{\circ}$. This angular interval covers the reflection pattern of the $\alpha\text{-Fe}$ - [0,1,1]-plane, $\gamma\text{-Fe}$ - [1,1,1]-plane, and $\text{Fe}_{23}(\text{C,B})_6$ phase- [1,1,5]-plane.

3. Results & discussion

3.1. Phase formation and transformations in solid state

The microstructural evolution starts with the solidification process. Fig. 1a) shows an isoplethal cross-section of the Fe-0.6C-B system. The hypoeutectic region is located in areas with B content below 3.4 mass\% . The microstructures analyzed in this study originate from this alloying region and display microstructures which

are characterized by primarily solidified iron dendrites surrounded by a eutectic structure (see Fig. 2). At a temperature of $T = 1147\text{ }^{\circ}\text{C}$, this structure results from the eutectic reaction **Liquid** $\rightarrow \gamma\text{-Fe} + \text{Fe}_2\text{B} + \text{Fe}_3(\text{B,C})$. At temperatures below $1147\text{ }^{\circ}\text{C}$ and B contents smaller than 3.1 mass\% , a phase field of $\gamma\text{-Fe} + \text{Fe}_3(\text{B,C})$ phases is present. In the temperature range between 900 and $600\text{ }^{\circ}\text{C}$, the $\text{Fe}_{23}(\text{C,B})_6$ phase (τ -phase) appears in equilibrium, overlapping with the temperature region of the $\gamma\text{-Fe} \rightarrow \alpha\text{-Fe}$ transition. Several multi-phase fields surround the $\alpha\text{-Fe} + \text{Fe}_{23}(\text{C,B})_6$ phase field, which are illustrated using a magnified scaling of the phase diagram in Fig. 1b) for the $600\text{--}1100\text{ }^{\circ}\text{C}$ temperature region and B contents up to 1.6 mass\% . It is clear that the formation of the $\text{Fe}_{23}(\text{C,B})_6$ phase results from a peritectoid decomposition of the $\text{Fe}_3(\text{B,C})$ -phase according to the reaction $\text{Fe}_3(\text{B,C}) + \text{Fe} \rightarrow \text{Fe}_{23}(\text{C,B})_6$ at descending temperatures and B contents smaller than 1.5 mass\% . Increasing B content subsequently stabilizes the Fe_2B phase. Thus the Fe_2B phase participates in the formation of the $\text{Fe}_{23}(\text{C,B})_6$ phase, according to the reaction $\text{Fe}_3(\text{B,C}) + \alpha\text{-Fe} \rightarrow \text{Fe}_{23}(\text{C,B})_6 + \text{Fe}_2\text{B}$. At temperatures below $750\text{ }^{\circ}\text{C}$ and B contents lower than 0.5 mass\% B, a phase field of $\alpha\text{-Fe} + \text{Fe}_3(\text{C,B})$ appears again. In this context, the label $\text{Fe}_3(\text{C,B})$ (as opposed to $\text{Fe}_3(\text{B,C})$) corresponds to a C-rich modification of the boron-cementite phase ($<10\text{ at.\% B}$), in contrast to the B-rich modification ($>20\text{ at.\% B}$) present at higher temperatures.

In Fig. 1b), the phases detected inside the microstructure of the analyzed alloys are marked with symbols. As illustrated in Fig. 1b), there is a clear deviation between equilibrium phase composition and phases detected inside the microstructure (see XRD diffractograms in Fig. 3). Particularly in the stability region of the τ -phase at tempering temperatures from $T = 700\text{--}800\text{ }^{\circ}\text{C}$, it is clear that the $\text{Fe}_3(\text{B,C})$ and Fe_2B phases are present in addition to the $\text{Fe}_{23}(\text{C,B})_6$ phase. Fig. 2a–f) shows the microstructures of the specimens tempered at $T = 700\text{ }^{\circ}\text{C}$ and $800\text{ }^{\circ}\text{C}$, illustrating that increasing B content further stabilizes the $\text{Fe}_3(\text{B,C})$ and Fe_2B phases present inside the coarsened eutectic structure beneath the $\text{Fe}_{23}(\text{C,B})_6$ phase. In addition, the $\text{Fe}_{23}(\text{C,B})_6$ phase is present in specimen 0.2B-0.6C- $700\text{ }^{\circ}\text{C}$, which is in contrast to the thermodynamic equilibrium which indicates the presence of C-rich modification of $\text{Fe}_3(\text{C,B})$ phase.

In solid state, the microstructural evolution and phase transformation processes originate from the solidification structure. Fig. 1 makes it clear that, in solid state, there is no homogeneous

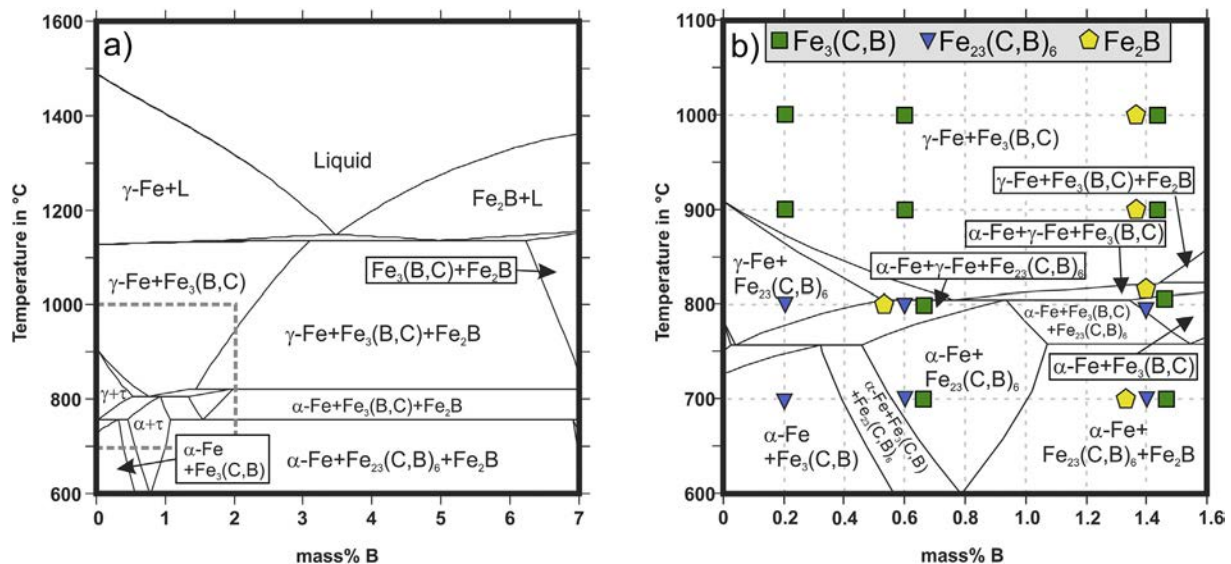


Fig. 1. a) Isothermal cross-section of the Fe-0.6C-B system calculated with ThermoCalc b) Symbols correspond to particular phases detected in the laboratory melts.

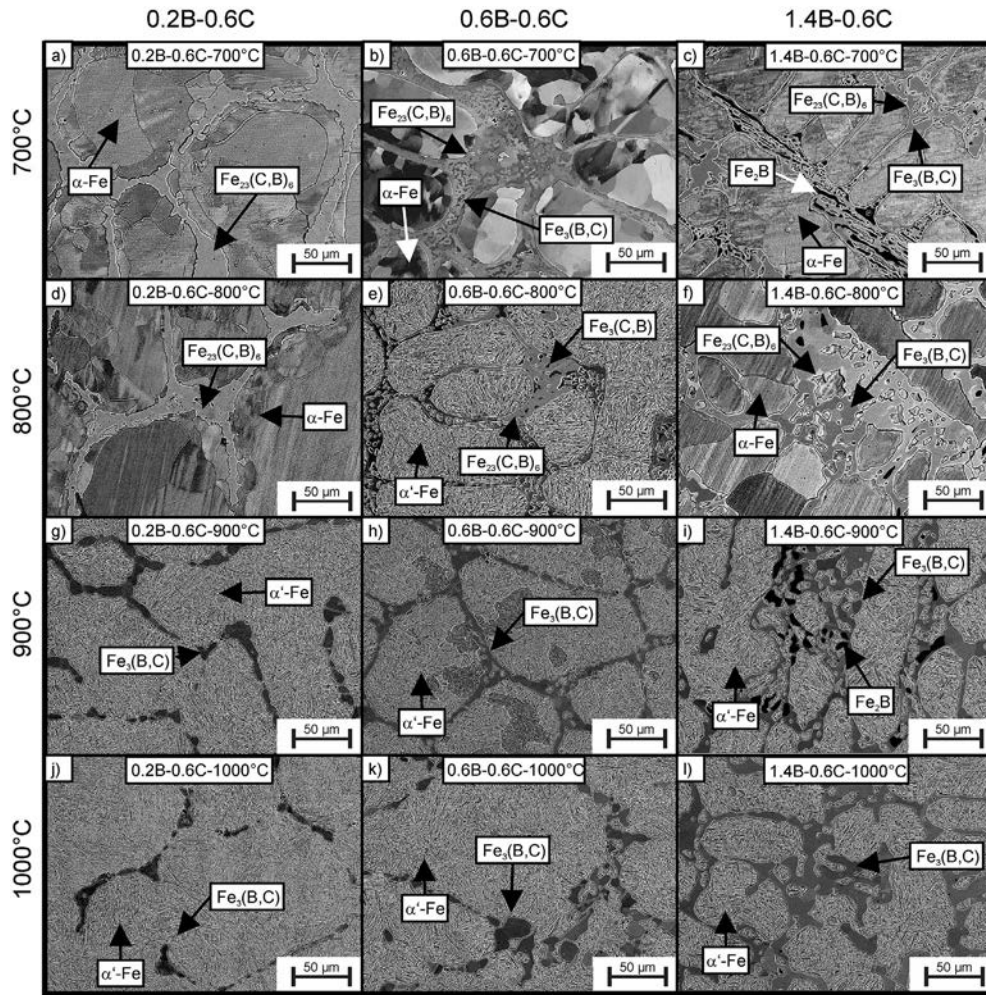


Fig. 2. SEM images (UA = 20 kV, BSE contrast) of the microstructures of samples 0.2B-0.6C, 0.6B-0.6C and 1.4B-0.6C, tempered at 700, 800, 900, and 1000 °C for 366 h and quenched in water, showing primary iron dendrites surrounded by eutectic carboborides/borides, which change structure according to the tempering temperature.

phase field of the iron matrix phase beneath the solidus temperature. This is because the Fe matrix only provides limited solubility for B (200–500 ppm). As a result, the agglomerations of eutectic borides ($\text{Fe}_3(\text{B,C}) + \text{Fe}_2\text{B}$) resulting from the solidification do not dissolve in solid state and are preserved inside the microstructure. The formation of the $\text{Fe}_{23}(\text{C,B})_6$ phase resulting from the decomposition of the $\text{Fe}_3(\text{B,C})$ phase at lower temperatures is particularly influenced by this solidification. Thus the $\text{Fe}_3(\text{B,C})$ phase can be considered the parental phase and initial structure for the $\text{Fe}_{23}(\text{C,B})_6$ phase formation/transformation. It will now be analyzed in detail.

3.1.1. The $\text{Fe}_3(\text{B,C})$ -phase as parental structure for $\text{Fe}_{23}(\text{C,B})_6$ formation

At temperatures of $T = 900$ °C and 1000 °C, the hard-phase network of the analyzed microstructures is mainly composed of the $\text{Fe}_3(\text{B,C})$ phase (see Fig. 2g, left). As shown in Fig. 4, the B content of the $\text{Fe}_3(\text{B,C})$ phase increases with the B content of the alloy. However, the WDS-measurement of the metalloid content of the $\text{Fe}_3(\text{B,C})$ phase shows a systematical offset of around +5 at.-% as compared to a stoichiometric composition of 25 at.-%. In a previous study the increase of B in the $\text{Fe}_3(\text{B,C})$ phase was related to micro-segregation processes during solidification. It was shown that the B enrichment of the eutectic structures is more significant as a consequence of technical, non-equilibrium solidification. In

addition, this micro-segregation behavior leads to the formation of B-rich Fe_2B phase inside the eutectic structure of alloys with a B/(C + B)-ratio higher than 0.625 (see alloy 1.4B-0.6C in Figs. 1b and 3) [11]. The measured composition of the Fe_2B phase is 35.28 ± 3.31 at.-% B 1.85 ± 0.5 at.-% C. Presuming stoichiometry of the Fe_2B phase, a systematic offset of the measured B content of 1.95 at.-% and C contamination of 1.85 at.-% can be conducted. Consequently, the measured B-content of the $\text{Fe}_3(\text{B,C})$ is increased around 2.7 at.-% as compared to equilibrium condition.

Taking into account the kinetics of the elements involved in the transformation of the respective hard phases, in solid state the local chemical, non-equilibrium composition of the eutectic structures can only be reduced to a limited extent. The coarse eutectic structures (10–100 μm) are an excessive accumulation of metalloid elements B and C; i.e., at $T = 1000$ °C the eutectic $\text{Fe}_3(\text{B,C})$ phase is composed of 5.4 mass% B and 2.3 mass% C in specimen 0.2B-0.6C-1000 °C, 6.3 mass% B and 1.8 mass% C in specimen 0.6B-0.6C-1000 °C, and 6.45 mass% B and 1.70 mass% C in specimen 1.4B-0.6C-1000 °C (see Fig. 4). Although the diffusivity of B in the iron lattice is high, its transport is restricted due to the marginal solubility of B (200–500 ppm) in the iron lattice, which leads to the instant formation of borides once this concentration is exceeded [12,13]. The diffusion kinetics of B and C inside these borides are several orders of magnitude lower [14–16]. Subsequently, the diffusion distance of B is limited and the chemical segregation which results from the

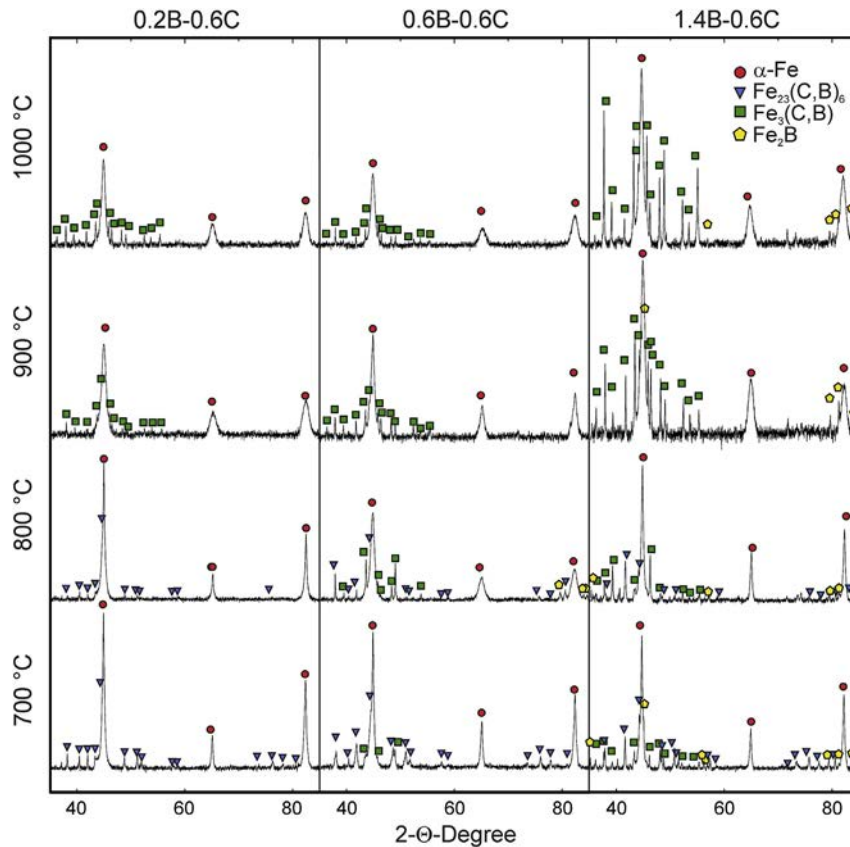


Fig. 3. XRD-diffractograms (Cu α -radiation, 35–85°2 θ , step size 0.1°) of alloys 0.2B-0.6C, 0.6B-0.6C, and 1.4B-0.6C tempered at the temperatures of 700, 800, 900, and 1000 °C for 366 h and quenched in water.

solidification is mostly preserved. Accordingly, in solid state the activated volume of the Fe matrix and therefore the phase fields corresponding to the thermodynamically relevant composition for the following phase formation processes can be found at C and B concentrations substantially higher than the overall alloying composition.

Fig. 5 shows isothermal cross-sections of the ternary Fe-C-B

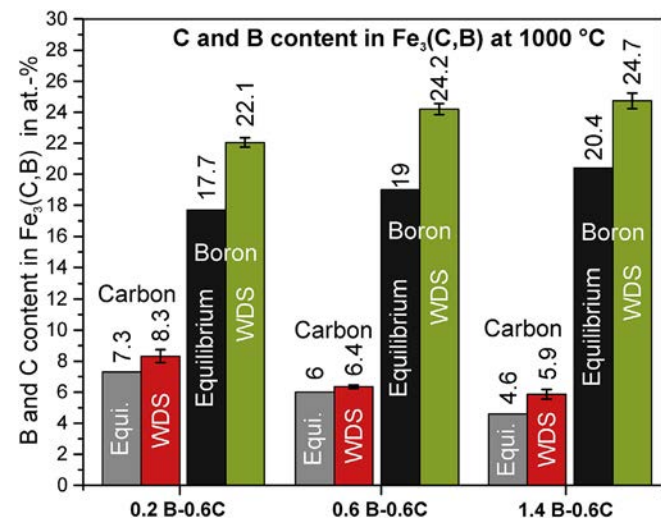


Fig. 4. C and B content of the $\text{Fe}_3(\text{B,C})$ phase at $T = 1000$ °C measured with WDS and calculated with TC for equilibrium condition.

system. The colored areas correspond to the concentration, which (depending on diffusion distance) levels out between the composition of the eutectic structure of $\text{Fe} + \text{Fe}_3(\text{B,C})$ reached by micro-segregation during solidification (red) and the respective composition of the $\text{Fe}_3(\text{B,C})$ phase measured in specimens tempered at 1000 °C (green). At temperatures of $T = 1000$ °C and 900 °C, a widespread phase field of γ -Fe and $\text{Fe}_3(\text{B,C})$ is present. In addition, both the average composition of the analyzed alloys and the composition of the eutectic structure correspond to the stability of the $\text{Fe}_3(\text{B,C})$ phase. At temperatures of $T = 800$ °C and 700 °C, the stability of the $\text{Fe}_{23}(\text{C,B})_6$ phase lies within a $\text{B}/(\text{C} + \text{B})$ ratio of 0.5–0.6, taking into account the B and C content available for forming hard phases (i.e., that which has not dissolved inside the iron matrix phase). Concerning the stability of the particular hard phase types in this temperature range, clear deviations occur between the corresponding phase field of average alloying composition (blue points) and local composition of the eutectic structures/phases (colored areas). The higher B contents inside the eutectic structures progressively stabilize the $\text{Fe}_3(\text{B,C})$ phase instead of the $\text{Fe}_{23}(\text{C,B})_6$ phase.

As a result of this preconditioning, the local B content of the parental, eutectic $\text{Fe}_3(\text{B,C})$ phase is increased, shifting the chemical composition and influencing the formation of the $\text{Fe}_{23}(\text{C,B})_6$ phase (at $T = 800$ °C and $T = 700$ °C) due to higher B content (see colored area in Fig. 5).

To summarize, in solid state, the formation and transformation of these phases are governed and limited by diffusion-controlled processes. The $\text{Fe}_3(\text{B,C}) \rightarrow \text{Fe}_{23}(\text{C,B})_6$ phase transformation depends on diffusion kinetics of the elements B and C, time, temperature, length scale, and local phase equilibria. The B content of

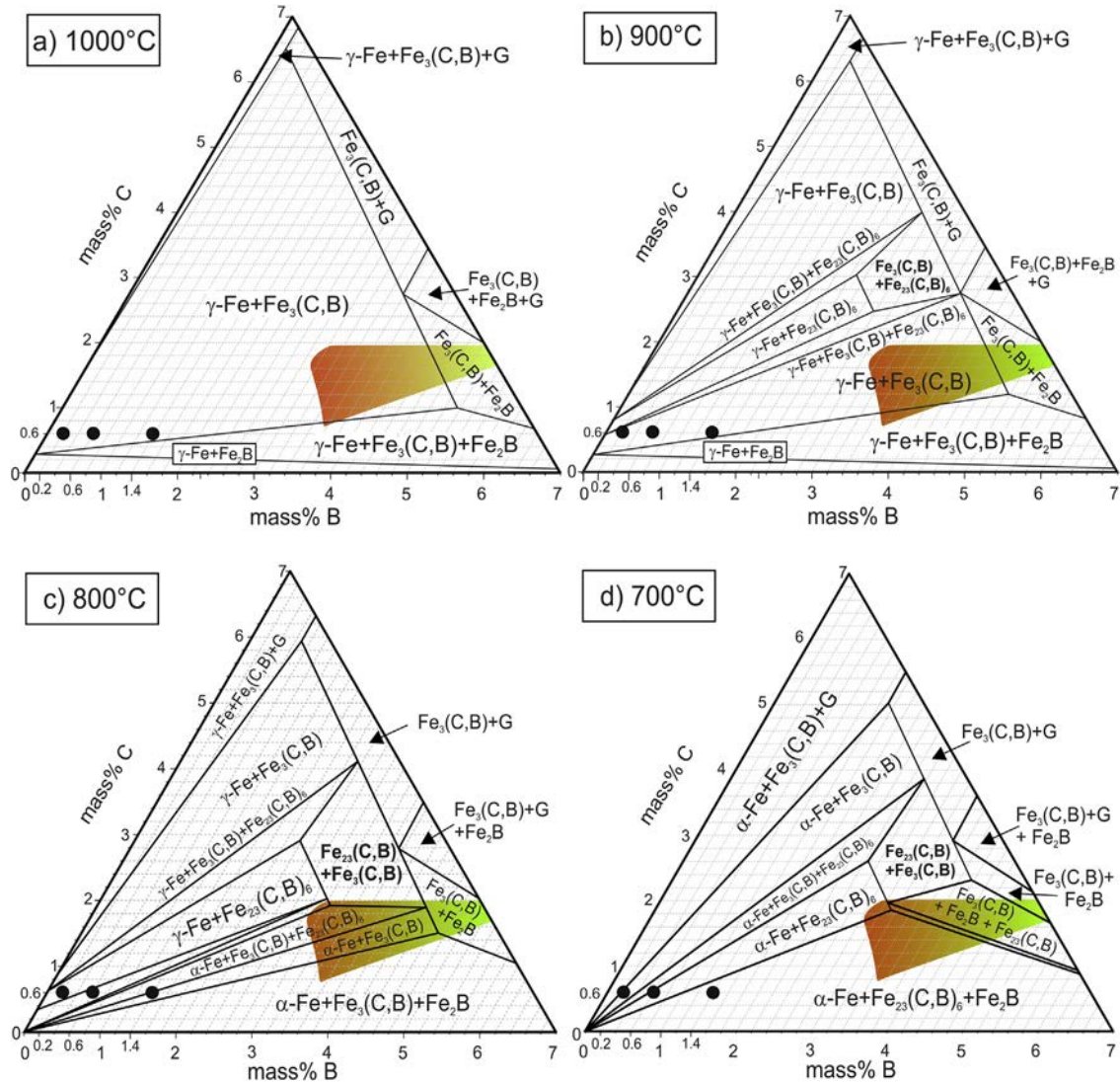


Fig. 5. Isothermal cross-section of the ternary Fe–C–B system calculated with ThermoCalc at temperatures of a) 1000 °C b) 900 °C c) 800 °C d) 700 °C. Nominal composition of the laboratory melts are marked with black points. The concentration range of the eutectic reaction, resulting from the micro-segregation during solidification, is marked as a red area, which in turn merges into the composition of the eutectic phases itself as measured by WDS (green area). (For interpretation of the references to colour in this figure legend, the reader is referred to the web version of this article.)

the Fe₃(B,C) phase, volume content/agglomeration of the Fe₃(B,C) phase, C content of the iron phase, and the crystal structure of the iron phase (α -Fe and/or γ -Fe) are important influencing parameters of the analyzed microstructures.

In Fig. 6, phase-quantity diagrams show that at temperatures above that needed for Fe₂₃(C,B)₆ formation, the volume fraction of the Fe₃(B,C) phase increases with the B content of the alloys. Image binarization was used to validate the Fe₃(B,C) phase content for specimens tempered at T = 900 °C. These show values of 4.8 ± 1.9 vol% in alloy 0.2B–0.6C; 16.7 ± 1.2 vol% in alloy 0.6B–0.6C and 33.5 ± 2.3 vol% in alloy 1.4B–0.6C, which agree with the equilibrium calculation. The agglomeration of the eutectic phases increases with increasing B content of the alloy, as is clear from the microstructures shown in Fig. 2. However, the C content of the iron matrix shows the opposite behavior, decreasing as the B content of the alloy increases. At a temperature of T = 900 °C, values of 0.5 mass% in alloy 0.2B–0.6C, 0.4 mass% in alloy 0.6B–0.6C, and 0.3 mass% in alloy 1.4B–0.6C were calculated for the C content solute in the γ -Fe matrix phase. This is connected to an increase of Fe₃(B,C) phase content and becomes evident through the position of the

particular alloying compositions in the phase field γ -Fe + Fe₃(B,C) in Fig. 5b). Connected to the C content of the iron phase, the stability of the austenite phase decreases as the B content of the alloy increases. Thus, at temperatures relevant for Fe₂₃(C,B)₆ formation, the iron matrix phase changes from a γ -Fe matrix in alloy 0.2B–0.6C, an α -Fe + γ -Fe phase in alloy 0.6B–0.6C (concurrent with γ -Fe → α -Fe transformation) to an α -Fe phase solely in the case of alloy 1.4B–0.6C.

3.1.2. Decomposition of the Fe₃(B,C) phase and formation of the Fe₂₃(C,B)₆ and Fe₂B phase

At temperatures of T = 800 °C and 700 °C, the Fe₃(B,C) phase becomes thermodynamically unstable regarding the nominal composition of the alloys analyzed. From a microstructural perspective, the formation of Fe₂₃(C,B)₆ phase starts with the nucleation of a Fe₂₃(C,B)₆ seed crystal, occurring at the interface between the Fe-matrix and Fe₃(B,C) phase, and decomposing according to the reaction $\text{Fe}_3(\text{B,C}) + \text{Fe} \rightarrow \text{Fe}_{23}(\text{C,B})_6$. The EBSD phase maps in Fig. 7 show that starting from a complete Fe₃(B,C) → Fe₂₃(C,B)₆ transformation in specimen 0.2B–0.6C–700 °C, increased

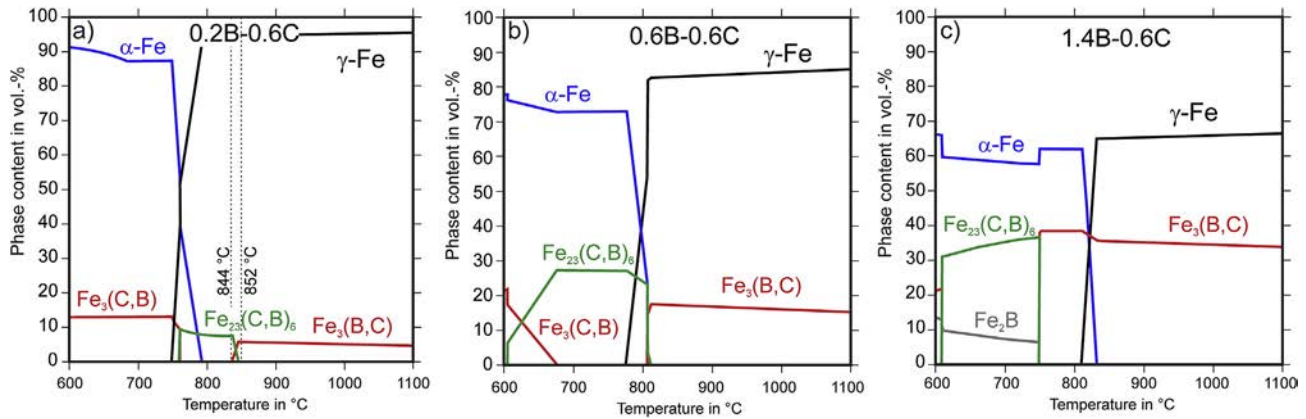


Fig. 6. Phase-quantity graphs calculated with ThermoCalc for the samples a) 0.2B-0.6C, b) 0.6B-0.6C, and c) 1.4B-0.6C.

B content leads to incomplete transformation and a retained $\text{Fe}_3(\text{B,C})$ phase inside the hard-phase structure. Unlike the TC calculation (see Fig. 1), this is a non-equilibrium effect. The retained $\text{Fe}_3(\text{B,C})$ phase is encased by a shell-like $\text{Fe}_{23}(\text{C,B})_6$ structure in specimen 0.6B-0.6C-700 °C and is subsequently present next to the B-rich Fe_2B phase in specimen 1.4B-0.6C-700 °C (see Fig. 7). The eutectic structure grows thicker with the increased volume content of boride phases with increasing B content of the alloy. However, a simultaneous decrease in the thickness of the $\text{Fe}_{23}(\text{C,B})_6$ layer which surrounds an increased phase content of the $\text{Fe}_3(\text{B,C})$ and Fe_2B phases in specimen 1.4B-0.6C-700 °C can be observed with increasing B content of the alloy (see Fig. 7c).

Fig. 8 illustrates the basic mechanisms involved in forming the $\text{Fe}_{23}(\text{C,B})_6$ phase. At first, in the $\text{Fe}/\text{Fe}_3(\text{B,C})$ interface the reaction $\text{Fe}_3(\text{B,C}) + \text{Fe} \rightarrow \text{Fe}_{23}(\text{C,B})_6$ takes place, whereby both $\text{Fe}_3(\text{B,C})$ phase and Fe matrix are consumed. Then the further transformation takes place at the newly formed $\text{Fe}_{23}(\text{C,B})_6/\text{Fe}_3(\text{B,C})$ and $\text{Fe}_{23}(\text{C,B})_6/\text{Fe}$ interfaces simultaneously. Accordingly, the front of transformation starts from the former $\text{Fe}/\text{Fe}_3(\text{B,C})$ interface and continues to grow in the direction of the Fe matrix and, due to its decomposition, also into the $\text{Fe}_3(\text{B,C})$ structure itself. The transformation of the $\text{Fe}_{23}(\text{C,B})_6$ phase then also consumes the $\text{Fe}_3(\text{B,C})$ phase in the newly formed $\text{Fe}_3(\text{B,C})/\text{Fe}_{23}(\text{C,B})_6$ interface. Consequently, the $\text{Fe}_{23}(\text{C,B})_6$ phase forms a shell-like structure which encloses the $\text{Fe}_3(\text{B,C})$ phase structure and separates it from the Fe matrix. The decomposition of the $\text{Fe}_3(\text{B,C})$ phase continues

according to the transformation reaction $\text{Fe}_3(\text{B,C}) \rightarrow \text{Fe}_{23}(\text{C,B})_6 + \text{B}$, with further B atoms released. The progression of the growth of the $\text{Fe}_{23}(\text{C,B})_6$ phase depends on the removal of B atoms from the $\text{Fe}_{23}(\text{C,B})_6/\text{Fe}_3(\text{B,C})$ interface and the supply of B and C atoms at the $\text{Fe}_{23}(\text{C,B})_6/\text{Fe}$ interface, and therefore depends on diffusion of the involved elements B and C. The released B atoms must diffuse through the $\text{Fe}_{23}(\text{C,B})_6$ layer to the interface of $\text{Fe}_{23}(\text{C,B})_6/\text{Fe}$ matrix. Throughout these processes, it is clear that the diffusion of C is necessary to form the C-rich $\text{Fe}_{23}(\text{C,B})_6$ phase, composed of between 14 and 16 at.-% B (3–3.6 mass% B) and 6–12 at.-% C (1.6–3.2 mass% C) (according to WDS measurements). The element C comes either from solid solution in the Fe matrix or from the $\text{Fe}_3(\text{B,C})$ phase itself. The release of B and partial C depletion of the remaining $\text{Fe}_3(\text{B,C})$ phase can be compensated by the formation of the B-rich Fe_2B phase if a critical limit of B is exceeded inside the $\text{Fe}_3(\text{B,C})$ phase. The formation of the Fe_2B phase is then promoted according to the schematic reaction $\text{Fe}_3(\text{B,C}) \rightarrow \text{Fe}_2\text{B} + \text{Fe}_{23}(\text{B,C})_6$ (see Fig. 7c).

In these processes, global equilibrium conditions are not reached due to the kinetic limitations in solid state; instead, local equilibrium conditions govern the phase formation. Taking into account the local composition of the eutectic $\text{Fe}_3(\text{B,C})$ phase for alloys 0.2B, 0.6B and 1.4B (as calculated for 1000 °C with ThermoCalc as shown in Fig. 4), schematic diffusion paths during the transformation processes are depicted in Fig. 9 in an isothermal cross-section of the Fe-C-B phase diagram at 700 °C. Depending on

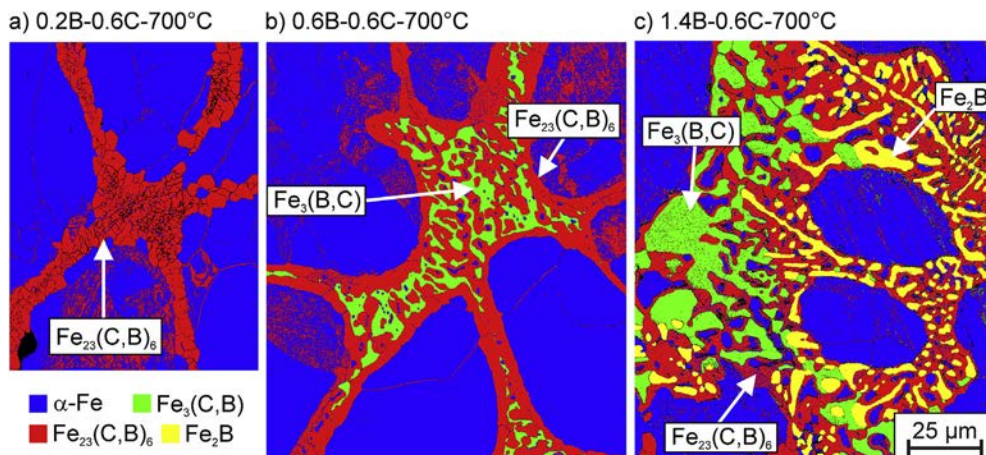


Fig. 7. EBSD phase maps of specimens 0.2B-0.6C, 0.6B-0.6C, and 1.4B-0.6C, which were annealed at 700 °C, step-size 0.15 µm, $U_A = 20$ kV.

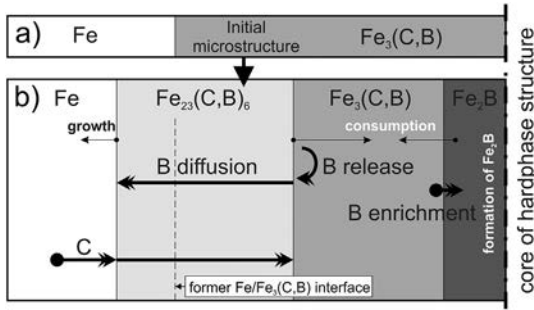


Fig. 8. Schematic illustration of the mechanisms influencing the $\text{Fe}_3(\text{B,C})/\text{Fe}_{23}(\text{C,B})_6$ transformation from a) an initial microstructure composed of Fe and $\text{Fe}_3(\text{B,C})$ as present at high temperatures to b) a shell-like microstructure of Fe, $\text{Fe}_{23}(\text{C,B})_6$, $\text{Fe}_3(\text{B,C})$ and Fe_2B in the core of the hard-phase structure as present at lower temperatures.

the local B content and local agglomeration of the $\text{Fe}_3(\text{B,C})$ phase, an increase of the activated $\text{B}/(\text{C} + \text{B})$ -ratio, as resulting from the diffusion processes, is observed with an increase of the nominal B content. In addition, as the transformation process progresses, the overall hard-phase content increases due to the higher $\text{M}/(\text{C} + \text{B})$ ratio of the $\text{Fe}_{23}(\text{C,B})_6$ phase ($\text{M}/(\text{C} + \text{B})$ ratio = 3.83) compared to the $\text{Fe}_3(\text{B,C})$ phase ($\text{M}/(\text{C} + \text{B})$ ratio = 3). This leads to a thickening of the hard-phase structure and thus to further limitation of the diffusion processes and increase in the diffusion distance of B and/or C from the remaining $\text{Fe}_3(\text{B,C})$ phase to the iron matrix. Thereby, the active $\text{B}/(\text{C} + \text{B})$ ratio of the alloys is shifted to higher values additionally, as the nominal B content of the alloys increases. This leads to different local equilibria which are connected to the stability of the $\text{Fe}_{23}(\text{C,B})_6$ phase in specimen 0.2B-0.6C-700 °C, $\text{Fe}_{23}(\text{C,B})_6 + \text{Fe}_3(\text{B,C})$ phases in specimen 0.6B-0.6C-700 °C and $\text{Fe}_{23}(\text{C,B})_6 + \text{Fe}_3(\text{B,C}) + \text{Fe}_2\text{B}$ or $\text{Fe}_{23}(\text{C,B})_6 + \text{Fe}_2\text{B}$ in specimen 1.4B-0.6C-700 °C.

3.1.3. Kinetics of the $\text{Fe}_3(\text{B,C}) \leftrightarrow \text{Fe}_{23}(\text{C,B})_6$ transformation

The formation of the $\text{Fe}_{23}(\text{C,B})_6$ phase here is similar to the growth of the FeB and Fe_2B type boride layers in the boriding

process and can be considered a kind of “inner boriding process”. The rate determining process is the diffusion of B through the boride layers; the kinetics can be described by parabolic growth according to $l = k\sqrt{t}$, where l is the phase/layer thickness, k is the growth rate constant, and t is the time. Given a particular temperature (roughly 800–1100 °C), time (order of magnitude 100 min), and chemical alloying composition, a boride layer thickness in the order of magnitude of 100 μm appears [14,16–20]. However, B is introduced using a boriding agent rather than released via phase decomposition and the rate determining factor is the low diffusion kinetics of B and C found inside the hard-phase structures themselves [13–15]. Thus, the $\text{Fe}_{23}(\text{C,B})_6$ layer acts as a kind of diffusion barrier and the kinetics of the $\text{Fe}_3(\text{B,C}) \rightarrow \text{Fe}_{23}(\text{C,B})_6$ transformation is progressively impeded.

In the following, the kinetics of the transformation from the $\text{Fe}_3(\text{B,C})$ to the $\text{Fe}_{23}(\text{C,B})_6$ phase is investigated using *in situ* XRD experiments for alloy 0.2B-0.6C, which shows a complete transformation of $\text{Fe}_3(\text{B,C}) \rightarrow \text{Fe}_{23}(\text{C,B})_6$ and thus displays no side effects due to retained $\text{Fe}_3(\text{B,C})$ or Fe_2B formation. From the phase quantity graph of sample 0.2B-0.6C (Fig. 6) and thermodynamic calculation (see Fig. 1a), it is clear that the transformation of $\text{Fe}_3(\text{B,C})$ (5 vol.-%) $\rightarrow \text{Fe}_{23}(\text{C,B})_6$ (8 vol.-%) occurs in a temperature range between 850 °C and 845 °C regarding equilibrium conditions. This is close to the temperature for $\gamma\text{-Fe}/\alpha\text{-Fe}$ transformation and thus relevant for the heat treatment of steels (e.g., hardening of tool steels). Again, taking into account equilibrium condition, at temperatures below 760 °C the $\text{Fe}_{23}(\text{C,B})_6$ phase dissolves in favor of the C-rich $\text{Fe}_3(\text{B,C})$ phase. However, as described in Section 3.1 the formation of the $\text{Fe}_{23}(\text{C,B})_6$ phase is governed by local equilibria thus leading to the stabilization of the $\text{Fe}_{23}(\text{C,B})_6$ phase in specimen 0.2B-0.6C-700 °C (see Fig. 7a). Thus it becomes evident from Fig. 5b), c), d) that the $\text{Fe}_{23}(\text{C,B})_6$ phase transformation temperature is affected by the active chemical composition of the eutectic structure. Fig. 10 depicts a isoplethal cross-section of the Fe-1.95C-B system, with regard to the average C content of the eutectic $\text{Fe}_3(\text{B,C})$ phase of 1.95 mass%. Fig. 10 illustrates that originating from complete stability of the $\text{Fe}_3(\text{B,C})$ phase at B contents > 4.2 mass% and temperatures

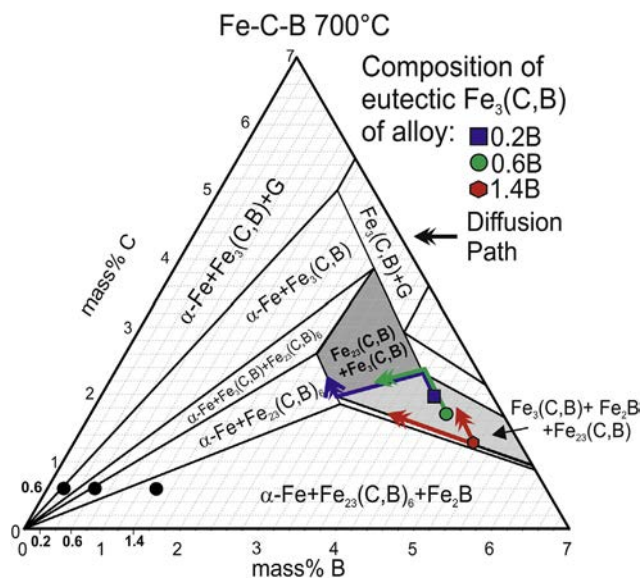


Fig. 9. Schematic illustration of possible diffusion paths during the $\text{Fe}_3(\text{B,C})/\text{Fe}_{23}(\text{C,B})_6$ transformation for the chemical composition of the eutectic $\text{Fe}_3(\text{B,C})$ phase in alloy 0.2B, 0.6B and 1.4B shown in an isothermal cross-section of the Fe-C-B phase diagram at 700 °C calculated with ThermoCalc.

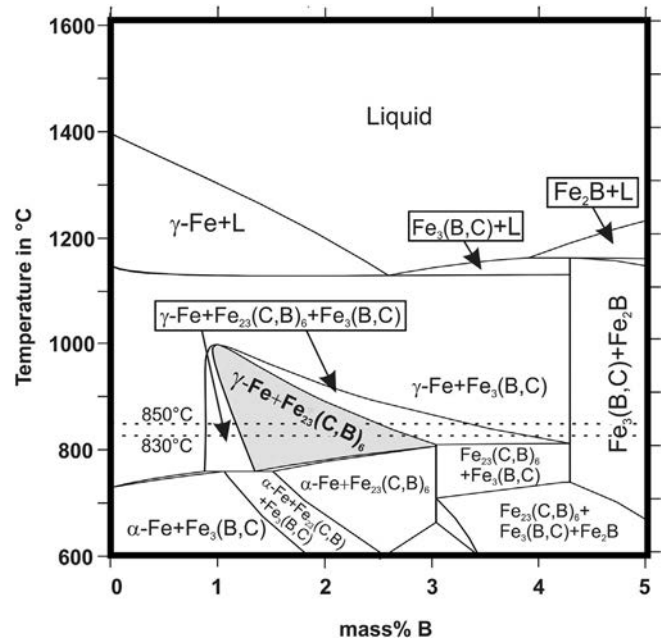


Fig. 10. Isolethal cross-section of the Fe-1.95C-B system with regard to the average C content of the eutectic $\text{Fe}_3(\text{B,C})$ phase calculated with ThermoCalc.

above 800 °C the formation temperature of the $\text{Fe}_{23}(\text{C,B})_6$ phase (phase field $\gamma\text{-Fe} \rightarrow \text{Fe}_{23}(\text{C,B})_6$) is increasing nearly to 1000 °C with diffusion and thus dilution of the element B from the eutectic structure (starting at B content < 5 mass%). In addition, it can be observed that the stability of the $\text{Fe}_{23}(\text{C,B})_6$ phase is extended to lower temperatures for local B contents higher than 2 mass%.

To map this transformation behavior during *in situ* XRD experiments, the temperature region between 850 °C (start of $\text{Fe}_{23}(\text{C,B})_6$ formation in equilibrium condition) and 830 °C (completion of $\text{Fe}_{23}(\text{C,B})_6$ formation in equilibrium condition) was crossed from high to low temperatures (see temperature profile in Fig. 11). The same temperature profile was then crossed backwards from low to high temperatures (see temperature profile in Fig. 12). Thereby, time = 0 min is defined as the first measurement at target temperature subsequently to the initial heating period. An initial hard-phase structure of the $\text{Fe}_3(\text{B,C})$ phase (see Fig. 2j) was adjusted by tempering the specimens for 24 h at 1000 °C using a vacuum furnace and subsequently quenching in water prior to experiments. To maintain a sufficient temporal resolution of the XRD measurement, the angular range was limited to between 42 and 46 2 θ° . Therefore, only separate reflections corresponding to particular phase orientations could be recorded. However, it can be assumed that the specimen surface features a sufficiently high number of different orientations, in spite of the texture conditioned by the solidification.

Fig. 13 shows diffractograms recorded for the temperature curve depicted in Fig. 11. During the 20 min heating up period from room temperature to 950 °C, the shape of the $\alpha\text{-Fe}$ -peak at 44.28 2 θ° constricted from being wide, elongated, and flat to a higher and narrower shape. This can be attributed to the stress relaxation of the martensitic matrix due to annealing effects. In addition, the $\alpha\text{-Fe}$ -peak slightly shifted to lower values of 2 θ° due to thermal expansion. On reaching a surface temperature of 950 °C, the $\alpha\text{-Fe} \rightarrow \gamma\text{-Fe}$ transformation was complete. The $\alpha\text{-Fe}$ peak disappeared and the peak at 42.76 2 θ° corresponding to $\gamma\text{-Fe}$ [111] reflection appeared. The temperature was kept constant at 950 °C for 20 min to allow homogenization of the microstructure. During this period no additional peak became evident in the 2 θ° -region of 42–46 2 θ° , showing that the microstructure (in agreement with the calculation in Fig. 6) is composed of $\gamma\text{-Fe}$ and the $\text{Fe}_3(\text{B,C})$ phase,

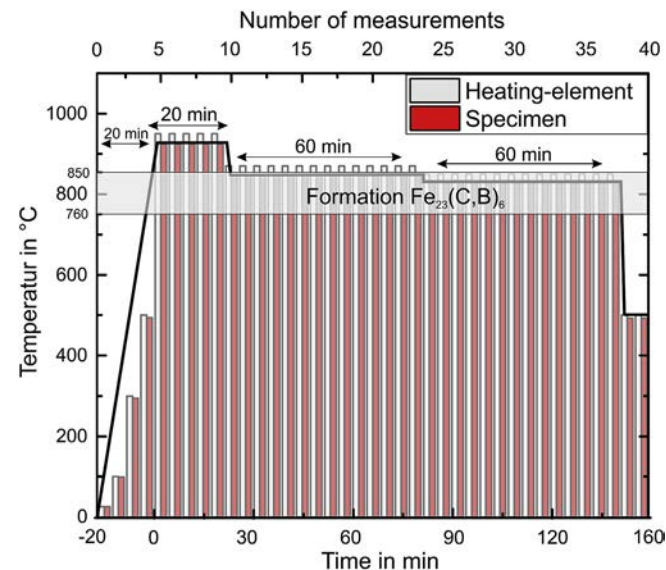


Fig. 11. Temperature curve of the *in situ* XRD experiment for the analysis of the formation of the $\text{Fe}_{23}(\text{C,B})_6$ phase during cooling.

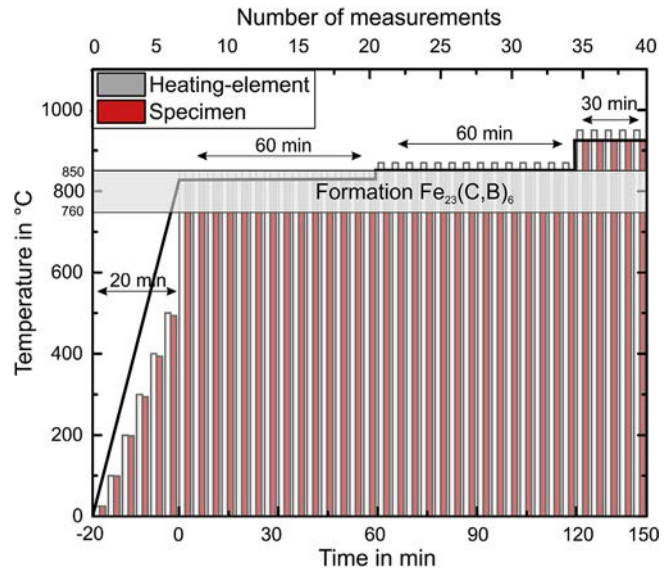


Fig. 12. Temperature curve of the *in situ* XRD experiment for the analysis of the formation of the $\text{Fe}_{23}(\text{C,B})_6$ phase during heating.

which does not show reflections in this region. Subsequently, the specimen was cooled down and kept at a constant surface temperature of 850 °C. During the first four measurements (16 min), the intensity of the $\gamma\text{-Fe}$ peak decreased slightly and the peak's position was shifted to a value of 42.84 2 θ° as a result of thermal expansion. Starting with the fifth measurement (20 min at 850 °C), a peak appeared at 44.06 2 θ° , which corresponds to the [511]-reflection of the $\text{Fe}_{23}(\text{C,B})_6$ phase. A thermal expansion of the lattice parameter a was observed, from 12.59 to 12.69 Å. The intensity of this peak increased in the following five measurements (periods of 20 min) and then remained constant after 40 min holding at 850 °C. After 60 min holding, the temperature of the specimen surface decreased to 830 °C. As a consequence of the temperature variation, the intensity of the $\text{Fe}_{23}(\text{C,B})_6$ phase peak increased slightly after the first measurement at 830 °C temperature (4 min) and remained constant for the subsequent 56 min holding period. Finally, the specimen temperature was further decreased to 500 °C, at which point the $\gamma\text{-Fe} \rightarrow \alpha\text{-Fe}$ transformation became visible. The $\text{Fe}_{23}(\text{C,B})_6$ phase peak shifted to a position of 44.10 2 θ° due to thermal expansion and a slight decrease in intensity.

Fig. 14 shows the diffractograms for the temperature curve shown in Fig. 12, with the specimen first heated from room temperature to 830 °C. On reaching the target temperature of 830 °C, the $\gamma\text{-Fe}$ peak appeared. The $\text{Fe}_{23}(\text{C,B})_6$ phase peak (44.06 2 θ°) appeared after a holding time of 4 min, and subsequently increased its intensity. A maximum peak intensity was reached after 60 min holding at 830 °C. Simultaneously, the intensity of the $\gamma\text{-Fe}$ phase peak at 42.84 2 θ° decreased. The temperature of the specimen was then increased to 850 °C. The $\text{Fe}_{23}(\text{C,B})_6$ phase peak then decreased in intensity and reached a constant level after 8–12 min holding at 850 °C. The intensity of the $\gamma\text{-Fe}$ phase peak then immediately increased again. After 60 min holding at 850 °C, the temperature increased to 950 °C. At this temperature, the $\text{Fe}_{23}(\text{C,B})_6$ phase peak disappeared after 12 min holding and the $\gamma\text{-Fe}$ phase peak further increased.

Comparing the transformation kinetics from the initial structure of $\text{Fe}_3(\text{B,C}) + \gamma\text{-Fe} \rightarrow \text{Fe}_{23}(\text{C,B})_6$ at the first temperature step of 850 °C during the cooling experiment (see Fig. 13) and 830 °C during the heating experiment (see Fig. 14) shows that the kinetics of transformation depend on undercooling ΔT in relation to the

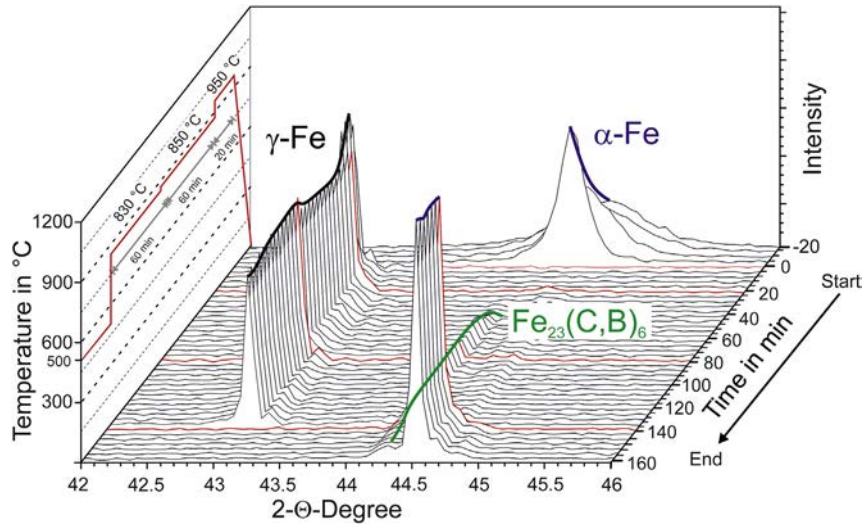


Fig. 13. High temperature XRD diffractograms of alloy 0.2B-0.6C recorded in time steps of 240 s corresponding to particular surface temperatures of the specimen (temperature profile in Fig. 11).

transformation temperature of $\text{Fe}_3(\text{B,C}) \rightarrow \text{Fe}_{23}(\text{C,B})_6$ and thus on the driving force for the phase formation. In contrast to the thermodynamic equilibrium calculations shown in Fig. 6a, the starting temperature of the phase formation shifted to higher temperatures. Taking into account the local chemical composition and the isoplethal cross-section shown in Fig. 10, it can be conducted that due to diffusion and B dilution an active B concentration between 2.5 and 3.5 mass% was reached. This concentration corresponds to a mutual phase field of $\text{Fe}_3(\text{B,C}) + \text{Fe}_{23}(\text{C,B})_6 + \gamma\text{-Fe}$ phases, where both phases show a coexistent stability and the temperature of 850 °C is slightly below the starting point of the phase transformation (low ΔT). In contrast, during the heating experiment at a temperature of 830 °C (high ΔT), the $\text{Fe}_3(\text{B,C}) + \gamma\text{-Fe} \rightarrow \text{Fe}_{23}(\text{C,B})_6$ transformation began after a holding time of 4 min. The $\text{Fe}_{23}(\text{C,B})_6$ phase peak did not settle at a constant value during the 60 min holding period. This may be attributed to lower diffusion kinetics and higher proportion of hard-phase structure undergoing the $\text{Fe}_3(\text{B,C}) + \text{Fe} \rightarrow \text{Fe}_{23}(\text{C,B})_6$ transformation, with the 830 °C

temperature step corresponding to the thermodynamic stability of the $\text{Fe}_{23}(\text{C,B})_6$ phase closer to, or inside the $\text{Fe}_{23}(\text{C,B})_6 + \gamma\text{-Fe}$ phase field. Furthermore, an incomplete description of the Fe-C-B system in the thermodynamic database TCFE7 has to be taken into account, which may lead to deviation of the calculation presented in this study and the experimental observation. However from the experiments it becomes evident that the $\text{Fe}_{23}(\text{C,B})_6$ phase formation depends on local equilibria, it is not stable at 950 °C but it is stable at 830 and 850 °C and at these temperatures appearing in different phase fractions. Independent of these effects, the increase in $\text{Fe}_{23}(\text{C,B})_6$ peak intensity was parabolic (for both temperature profiles), which corresponds to the progressive impediment of the diffusion kinetics of B and C through the growing $\text{Fe}_{23}(\text{C,B})_6$ layer.

Comparing the increase in $\text{Fe}_{23}(\text{C,B})_6$ phase fraction occurring after cooling from 850 °C to 830 °C (transition from the first to the second temperature step in Fig. 13) shows that the transformation was complete after 4 min following the reaction $\text{Fe}_3(\text{B,C}) + \gamma\text{-Fe} \rightarrow \text{Fe}_{23}(\text{C,B})_6$. A longer period was needed to dissolve the $\text{Fe}_{23}(\text{C,B})_6$

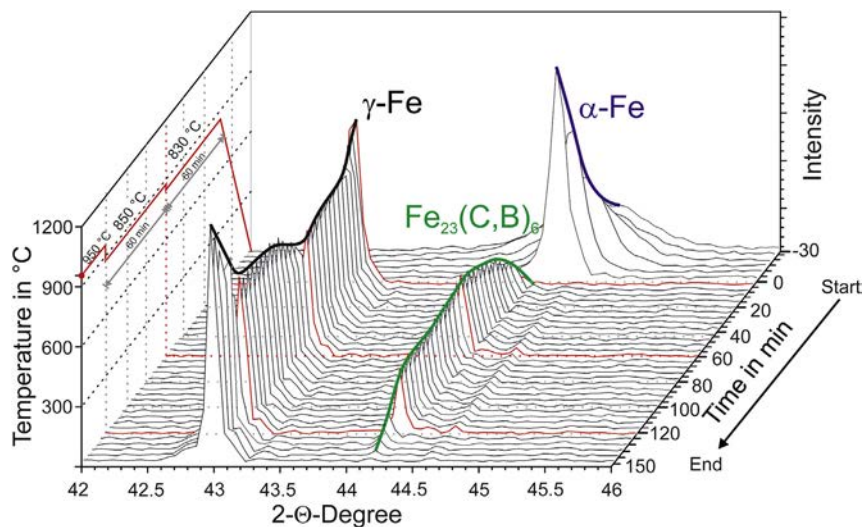


Fig. 14. High temperature XRD diffractograms of alloy 0.2B-0.6C recorded in time steps of 240 s corresponding to particular surface temperatures of the specimen (temperature profile in Fig. 12).

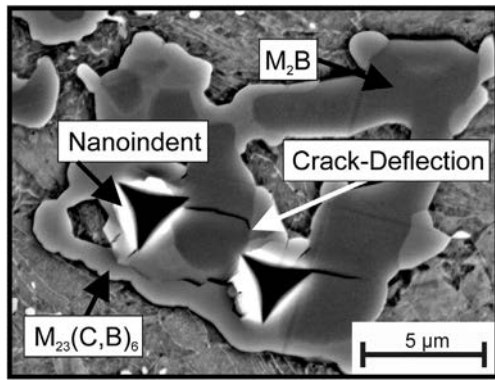


Fig. 15. Deflection of a crack induced by a nanoindent in a multiphased hard-phase structure in alloy 0.6C-0.6B-10Cr tempered at 1000 °C.

phase during heating from 830 °C to 850 °C, which was completed after a period of 8–12 min, following the reaction $\text{Fe}_{23}(\text{C,B})_6 \rightarrow \text{Fe}_3(\text{B,C}) + \gamma\text{-Fe}$. Twelve min were also needed to dissolve the $\text{Fe}_{23}(\text{C,B})_6$ phase at 950 °C, again following the reaction $\text{Fe}_{23}(\text{C,B})_6 \rightarrow \text{Fe}_3(\text{B,C}) + \gamma\text{-Fe}$ (see Fig. 13).

3.1.4. Relevance for alloy design

This study described the basic mechanisms involved in the solid-state transformation of the eutectic borides present in the hypoeutectic region of the Fe-C-B system and thus can be used as a basis for further alloy design in this system. It was shown that the microstructure is strongly preconditioned by B enrichment during solidification. Subsequently, depending on the B/(C + B) ratio of the particular eutectic $\text{Fe}_3(\text{B,C})$ phase, different local equilibrium conditions are relevant for the $\text{Fe}_3(\text{B,C}) \rightarrow \text{Fe}_{23}(\text{C,B})_6$ transformation. In addition, phase transformation of the eutectic hard phases takes place during a temperature range and timeframe relevant for the heat treatment/annealing of tool steels. Thus, all the processes described above must be taken into account when processing tool steels based on the ternary Fe-C-B system. In particular, during annealing at $T < 800$ °C the $\text{Fe}_3(\text{B,C}) \rightarrow \text{Fe}_{23}(\text{C,B})_6$ transformation leads to an increase in the volume fraction of the hard phases and thus to a decrease in fracture toughness and embrittlement of the alloy. Furthermore, the martensitic hardenability of the iron matrix can be decreased by increased solute C inside the $\text{Fe}_{23}(\text{C,B})_6$ phase during the phase transformation. By controlling and taking into account these processes in a novel alloying approach, the proposed findings can be used to adjust a multi-phased hard-phase structure (e.g., Fe_2B , $\text{Fe}_3(\text{C,B})$, and $\text{Fe}_{23}(\text{C,B})_6$), which is promising for increasing the fracture toughness of the eutectic structure itself, due to increased density of interfaces and deflection of cracks. Also the rather metallic character of $\text{Fe}_{23}(\text{C,B})_6$ phase can lead to improved embedding of the hard-phases of Fe_2B and $\text{Fe}_3(\text{B,C})$ inside the iron matrix. As an example, Fig. 15 illustrates the deflection of a crack induced by a nanoindent in a hard-phase structure composed of M_2B and $\text{M}_{23}(\text{C,B})_6$ in a different alloy which includes 10 mass% Cr to stabilize the $\text{M}_{23}(\text{C,B})_6$ to higher temperatures.

4. Summary and conclusion

This study investigated the solid state transformations of the $\text{Fe}_3(\text{B,C})$ and $\text{Fe}_{23}(\text{C,B})_6$ phases occurring in the hypoeutectic Fe-C-B system. Thermodynamic equilibrium calculations were used and experimentally validated, with the following results:

- Solid-state transformations in the hypoeutectic region of the Fe-C-B system are influenced by an enrichment of B inside the

eutectic structure resulting from the solidification process. This increased B content is not reduced in solid state due to the low diffusivity of B and C inside the hard-phase structure and the low solubility of B in the metal matrix.

- Phase stability is subject to local equilibria related to the local C and B concentration of the hard-phase structure.
- At $T = 900$ and 1000 °C, small amounts of the Fe_2B phase are present in addition to the $\text{Fe}_3(\text{B,C})$ hard phase in alloys with increasing B content.
- In the temperature range from $T = 700$ °C– 800 °C, a peritectoid decomposition of the $\text{Fe}_3(\text{B,C})$ phase occurs according to the schematic reaction $\text{Fe}_3(\text{B,C}) + \text{Fe} \rightarrow \text{Fe}_{23}(\text{C,B})_6$ or at higher B/(C + B) ratios according to $\text{Fe}_3(\text{B,C}) \rightarrow \text{Fe}_{23}(\text{C,B})_6 + \text{Fe}_2\text{B}$
- Increasing B content subsequently stabilizes the $\text{Fe}_3(\text{B,C})$ and Fe_2B phases, which are then present in addition to the $\text{Fe}_{23}(\text{C,B})_6$ phase.
- In this process, the $\text{Fe}_{23}(\text{C,B})_6$ phase forms a shell-like structure surrounding the $\text{Fe}_3(\text{B,C})$ and/or Fe_2B phases, which impedes the further decomposition of the $\text{Fe}_3(\text{B,C})$ phase.
- The kinetics of the $\text{Fe}_3(\text{B,C}) + \text{Fe} \rightarrow \text{Fe}_{23}(\text{C,B})_6$ reaction was investigated using high-temperature *in situ* XRD experiments, where it was found that the transformation is completed in 40–60 min, depending on temperature and undercooling.

Acknowledgment

The authors gratefully acknowledge financial support from the Deutsche Forschungsgemeinschaft (DFG) within the project “Boron-alloyed Tool Steels” RO 4523/2–1.

References

- [1] A. Röttger, J. Lentz, W. Theisen, Boron-alloyed Fe–Cr–C–B tool steels — Thermodynamic calculations and experimental validation, *Mater. Des.* 88 (2015) 420–429.
- [2] J. Lentz, A. Röttger, W. Theisen, Gefügeausbildung und mikromechanische Eigenschaften einzelner Phasen von untereutektischen Fe-C-B Legierungen, in: S. Mayer, M. Panzenböck, H. Clemens (Eds.), *Fortschritte in der Metallographie*, INVENTUM GmbH, Bonn, 2014, pp. 283–288.
- [3] H. Berns, *Hartlegierungen und Hartverbundwerkstoffe: Gefüge, Eigenschaften, Bearbeitung, Anwendung*, Springer, Berlin, 1998.
- [4] P. Rogl, Boron – carbon – iron, in: W. Martienssen, G. Effenberg, S. Ilyenko (Eds.), *Iron Systems, Part 1*, Springer Berlin Heidelberg, Berlin, Heidelberg, 2008, pp. 349–378.
- [5] C.R. Das, S.K. Albert, J. Swaminathan, A.K. Bhaduri, B.S. Murty, Effect of boron on creep behaviour of inter-critically annealed modified 9Cr-1Mo steel, *Procedia Eng.* 55 (2013) 402–407.
- [6] K.S. Chandravathi, K. Laha, N. Shinya, M.D. Mathew, Effects of boron and cerium on creep rupture properties of modified 9Cr-1Mo steel and its weld joint, *Procedia Eng.* 55 (2013) 433–437.
- [7] F. Abe, Effect of boron on microstructure and creep strength of advanced ferritic power plant steels, *Procedia Eng.* 10 (2011) 94–99.
- [8] B. Hwang, D.-W. Suh, S.-J. Kim, Austenitizing temperature and hardenability of low-carbon boron steels, *Scr. Mater.* 64 (2011) 1118–1120.
- [9] W. Stumpf, K. Banks, The hot working characteristics of a boron bearing and a conventional low carbon steel, *Mater. Sci. Eng. A* 418 (2006) 86–94.
- [10] J. Bok Seol, G. Ho Gu, N. Suk Lim, S. Das, C. Gyung Park, Atomic scale investigation on the distribution of boron in medium carbon steels by atom probe tomography and EELS, *Ultramicroscopy* 110 (2010) 783–788.
- [11] J. Lentz, A. Röttger, W. Theisen, Solidification and phase formation of alloys in the hypoeutectic region of the Fe–C–B system, *Acta Mater.* 99 (2015) 119–129.
- [12] W. Wang, S. Zhang, X. He, Diffusion of boron in alloys, *Acta Metall. Mater.* 43 (1995) 1693–1699.
- [13] J. Pelleg, M. Judelewicz, Diffusion in the B- α -Fe system and compound formation between electron gun deposited boron thin films and steel substrate, *Thin Solid Films* 215 (1992) 35–41.
- [14] I. Campos, G. Ramírez, U. Figueroa, J. Martínez, O. Morales, Evaluation of boron mobility on the phases FeB , Fe_2B and diffusion zone in AISI 1045 and M2 steels, *Appl. Surf. Sci.* 253 (2007) 3469–3475.
- [15] A. Brown, J. D. Garnish, R.W.K. Honeycombe, The distribution of boron in pure iron, *Metal. Sci.* 8 (1974) 317–324.
- [16] L. Yu, X. Chen, K. Khor, G. Sundararajan, FeB/FeB phase transformation during SPS pack-boriding, *Acta Mater.* 53 (2005) 2361–2368.
- [17] V.I. Dybkov, L.V. Goncharuk, V.G. Khoruzha, K.A. Meleshevich, A.V. Samelyuk,

- V.R. Sidorko, Diffusional growth kinetics of boride layers on iron-chromium alloys, *SSP* 138 (2008) 181–188.
- [18] V. Sista, O. Kahvecioglu, O.L. Eryilmaz, A. Erdemir, S. Timur, Electrochemical boriding and characterization of AISI D2 tool steel, *Thin Solid Films* 520 (2011) 1582–1588.
- [19] I. Campos-Silva, M. Ortiz-Domínguez, M. Keddam, N. López-Perrusquia, A. Carmona-Vargas, M. Elías-Espinosa, Kinetics of the formation of Fe₂B layers in gray cast iron: effects of boron concentration and boride incubation time, *Appl. Surf. Sci.* 255 (2009) 9290–9295.
- [20] I. Campos-Silva, M. Ortiz-Domínguez, O. Bravo-Bárceñas, M.A. Doñu-Ruiz, D. Bravo-Bárceñas, C. Tapia-Quintero, M.Y. Jiménez-Reyes, Formation and kinetics of FeB/Fe₂B layers and diffusion zone at the surface of AISI 316 borided steels, *Surf. Coat. Tech.* 205 (2010) 403–412.